BIOPHYSICS

Excess surface area of the nuclear lamina enables unhindered cell migration through constrictions

Brendan McKee[1]†, Samere Abolghasemzade[1]†, Ting-Ching Wang[2], Kajol Harsh[1], Simran Kaur[1], Ryan Blanchard[1], Krishna Belraj Menon[1,3], Mohammad Mohajeri[1], Richard B. Dickinson[4]*, Tanmay P. Lele[1,2,5,6]*

Cell migration through narrow spaces is essential in wound healing and metastatic spread of cancer. Cells must deform the large nucleus to fit through constricting channels. To understand the role of the nuclear lamina in limiting cell migration through constrictions, we imaged it in cells migrating through periodic constricting channels in a microdevice. The lamina underwent cycles of wrinkling and smoothing as the nucleus changed from an irregular, rounded shape in the wide channel regions between constrictions to a smooth, hourglass shape as the nucleus passed through the center of a constriction. The laminar surface area of nuclei within constrictions was measured to be at or above the computationally predicted threshold area for the nuclear volume. The channels excluded control nuclei that had insufficient excess surface area, but not nuclei lacking lamin A/C. Thus, the excess surface area of the nuclear lamina enables cell migration through constricting channels.

INTRODUCTION

Physiological processes, such as wound healing, and pathological processes, such as cancer metastasis, involve the migration of cells through narrow constrictions in the interstitial tissue (*1*, *2*). To be able to migrate through constrictions that are smaller than the nuclear size, cells must deform the nucleus (*3*–*6*). The nuclear lamina, which is composed of A-type and B-type lamins, largely determines the resistance of the nucleus to deformation. Lower levels of lamin A/C allow facile nuclear deformation and promote cell migration through constrictions in the tissue interstitium (*7*–*9*), contributing to tumor metastasis (*10*). How the nuclear lamina mechanically limits its migration through narrow constrictions is not fully understood.

Mechanical models of nuclear deformation typically assume that the nucleus deforms from the starting shape of a sphere (*11*–*15*). However, the nucleus intrinsically has excess surface area in the nuclear lamina (over that of a sphere of the same volume), which is observed as wrinkles in the nuclear surface when the overall shape of the nucleus is rounded (*16*, *17*). The shape of a rounded nucleus that has excess area in the lamina can be changed without causing an in-plane extensional strain in the lamina, as the wrinkles will simply become smoothed out (*16*). When the lamina becomes fully taut, it remains nearly inextensible to cellular force scales but supports an in-plane tension that will balance nuclear pressure (*16*). These are the main features of our recently proposed nuclear drop model (*18*–*21*). In this model, nuclear deformation under force is determined almost entirely by resistance to surface area expansion and to volume compression, rather than any resistance to shear deformation of the nuclear contents (*22*).

The nuclear drop model predicts threshold-like behavior (*16*, *19*), such that the nucleus is compliant when the lamina has wrinkles in it and becomes stiff to further deformation when the lamina is smooth and taut. Thus, the nuclear drop model predicts that excess surface area of the nuclear lamina allows large nuclear deformations to occur without expansion of the laminar surface area or compression of the nuclear volume—up to the point where the lamina becomes smooth and taut, thereby stiffening the nucleus to further deformation.

In the context of cell migration, the nuclear drop model anticipates that only nuclei with sufficient excess surface area will pass through constrictions without requiring volume compression or laminar expansion. In the extreme case of a perfectly spherical nucleus, the nucleus would never fit into a constriction of a size lower than the sphere diameter under the constraint of constant volume and surface area. However, with sufficient excess surface area, the nucleus would be able to deform to fit through narrow constrictions. Thus, the amount of excess area should set a threshold on whether the nucleus can pass through a constriction with minimal mechanical resistance.

Here, we tested the above predictions of the nuclear drop model by tracking the nuclear lamina as cells entered and exited narrow constrictions. To enable repeated tracking of the same nucleus during migration, we modified a microdevice previously developed by Lammerding and coworkers (*23*) and performed high-resolution imaging of the same nucleus as it underwent single file motion through periodic constrictions. We quantified area of the nuclear lamina along with three-dimensional (3D) nuclear shapes during the migration and compared them to corresponding predictions of a computational model. We found that the laminar surface area of nuclei within constrictions was consistently at or above the computationally predicted threshold area for the nuclear volume, and the channels excluded nuclei that had insufficient excess surface area to pass through constrictions. These results suggest that excess area in the nuclear lamina enables cell migration through narrow constrictions, consistent with the predictions of the nuclear drop model.

RESULTS

We fabricated a polydimethylsiloxane (PDMS)–based microdevice that maintains a gradient of growth factor for promoting migration of cells through constricting channels (Fig. 1A and fig. S1). The design allows the tracking of single cells as they migrate through repeated

[1]Department of Biomedical Engineering, Texas A&M University, College Station, TX 77843, USA. [2]McFerrin Department of Chemical Engineering, Texas A&M University, College Station, TX 77843, USA. [3]Indian Institute of Science Education and Research, Pune, Maharashtra 411008, India. [4]Department of Chemical Engineering, University of Florida, Gainesville, FL 32611, USA. [5]Department of Translational Medical Sciences, Texas A&M University, College Station, TX 77843, USA. [6]Texas A&M University School of Engineering Medicine, 1020 Holcombe Blvd, Houston, TX 77030, USA.
*Corresponding author. Email: dickinso@ufl.edu (R.B.D.); tanmay.lele@tamu.edu (T.P.L.)
†These authors contributed equally to this work.

constrictions (Fig. 1, B and C). F-actin staining showed that cells tended to expand to the width of the channel and spanned more than one constriction (Fig. 1D). We performed high-resolution imaging of an HT-1080 fibrosarcoma cell line that stably expresses green fluorescent protein (GFP) fused to barrier-to-autointegration factor (BAF). This DNA binding protein localizes to the nuclear envelope and is a reporter of nuclear envelope rupture. The GFP-BAF expressing nuclear shapes revealed the presence of free, smooth surfaces on either side of the 3- and 8-μm–width constrictions (Fig. 1E). These smooth surfaces are consistent with a pressure difference across the envelope balanced by tension in the curved nuclear surface according to the Law of Laplace. Localized high-intensity GFP-BAF spots on the membrane indicating nuclear rupture were generally not observed, although a small fraction of nuclei (~10%) did undergo rupture in the 3-μm–width constrictions (movie S1); rupture was essentially absent in the 8-μm–width constrictions. Nuclear rupture was also detected by cyclic guanosine 5′-monophosphate (GMP)–adenosine 5′-monophosphate (AMP) synthase (cGAS)

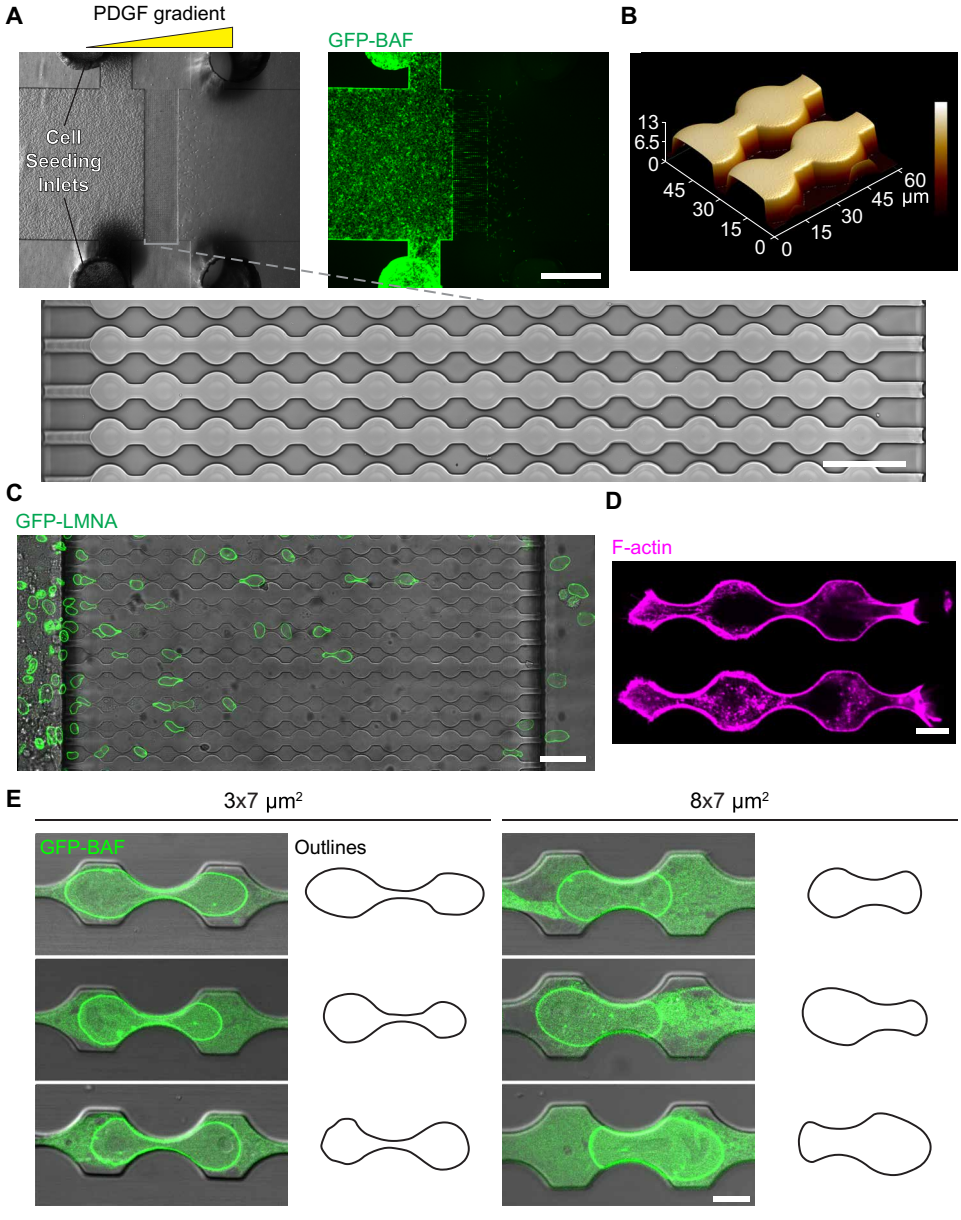

Fig. 1. Nuclei undergo drop-like deformation during confined migration. (**A**) Confocal images show the central channel and cell seeding inlets of the confining device (top). HT-1080 cells expressing GFP-BAF (green) were seeded on the left side of the channel and migrated across the channel, driven by a PDGF gradient. Scale bar, 1 mm. An enlarged view shows the channel design with 15 consecutive constrictions. Scale bar, 50 μm. (**B**) Atomic force microscopy image showing the 3D profile of a fabricated device with 3 μm–by–7 μm constrictions. (**C**) Confocal image shows HT-1080 cells expressing GFP-LMNA (i.e., GFP-lamin A/C) (green) migrating through 2 μm–by–7 μm constrictions. Scale bar, 50 μm. (**D**) Confocal image shows F-actin staining in an HT-1080 cell within the confining channel. Scale bar, 10 μm. (**E**) Confocal images show HT-1080 cells expressing GFP-BAF (green) confined in 3 μm–by–7 μm and 8 μm–by–7 μm constrictions. Nuclear outlines on the right show the nuclear contour within the constrictions. Scale bar, 10 μm.

immunostaining (fig. S2), which showed that ~8% of cells rupture in 3 μm–by–7 μm constrictions, ~21% in 2 μm–by–7 μm constrictions, and ~0% in 8 μm–by–7 μm constrictions.

To track changes in the nuclear lamina during repeated constriction, we used confocal fluorescence microscopy to image HT-1080 cells expressing GFP-tagged lamin A/C as they migrated through the constrictions. Consistent with the drop model, the nuclear lamina showed cycles of smoothing during constriction, followed by wrinkling after exiting from the constriction (Fig. 2A and movie S2). Thus, a transition from a round nucleus to an hourglass-shaped nucleus in the constriction smooths the nuclear lamina, followed by the recovery of the wrinkles as the nucleus rounds in exiting the constriction. Notably, the initially wrinkled nuclei did not revert to the same shapes following passage through the constriction; thus, elastic energy is not stored in the nuclear shape on the timescale of cell migration (*22*). Nuclear smoothing required narrow constrictions; nuclei in constrictions wider than a cross-sectional area of 8 μm by 7 μm did not always smooth fully in the constriction (Fig. 2B).

We quantified the wrinkling and smoothing in the nuclear lamina, along with the positions of the centroid, back edge, and front edge of the nucleus. The nucleus proceeded through a step-wise

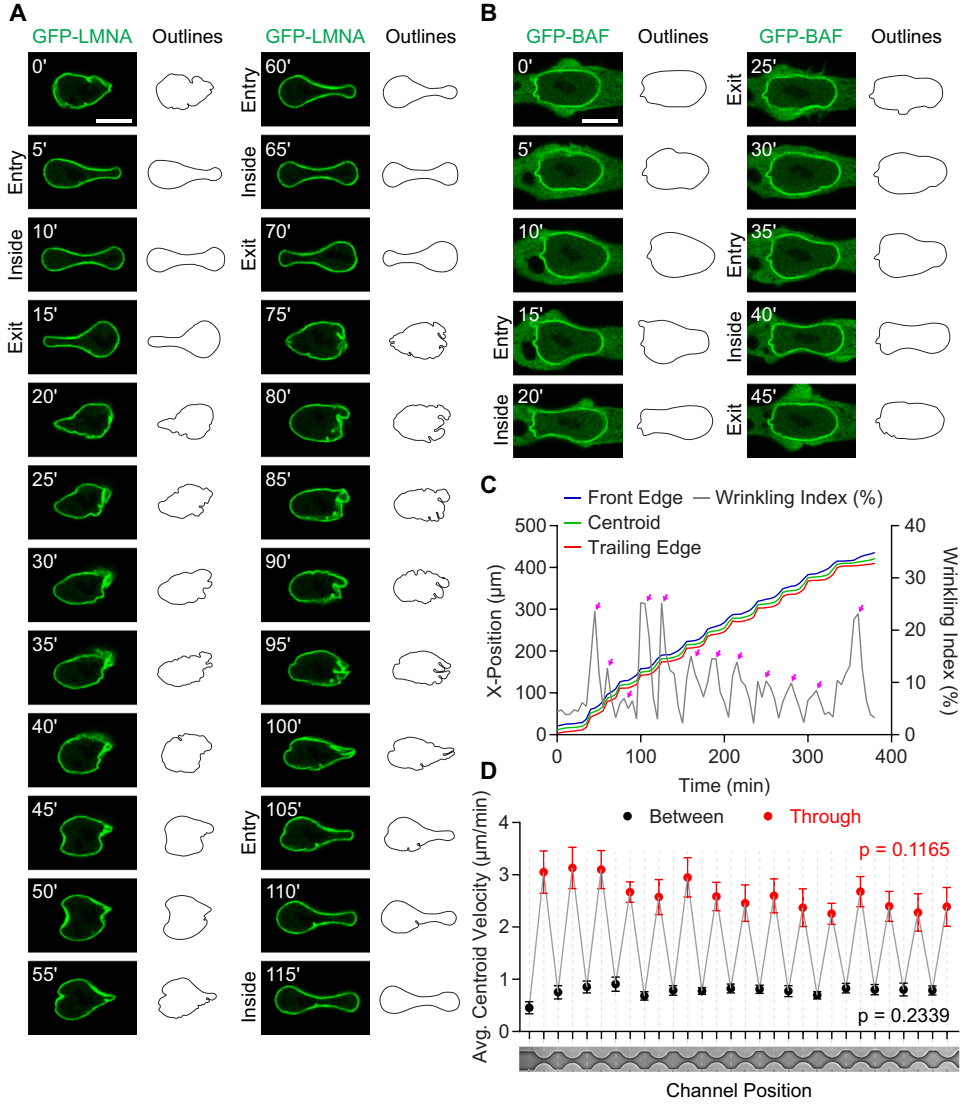

Fig. 2. Laminar unwrinkling and wrinkling cycles during migration through periodic constrictions. (**A**) Time-lapse confocal images show the nucleus of an HT-1080 cell expressing GFP-LMNA (green) as the cell migrated through consecutive 3 μm–by–7 μm constrictions. Nuclear outlines on the right depict the shapes. Scale bar, 10 μm. (**B**) Time-lapse confocal images show an HT-1080 nucleus expressing GFP-BAF (green) as the cell migrated through consecutive 8 μm–by–7 μm constrictions. Nuclear outlines are shown on the right. Scale bar, 10 μm. (**C**) Measurements of nuclear front edge (blue), centroid (green), and trailing (red) edge positions over time show a step-like nuclear motion. Rapid acceleration occurred as the nucleus escaped constriction, which coincided with the subsequent increase of the wrinkling index (gray; peaks labeled with magenta arrows). (**D**) Average centroid velocity of nuclei as they migrated through 3 μm–by–7 μm channels shows a cyclic pattern. Maximum and minimum speeds stayed roughly constant across the repeating constrictions. Error bars are standard error of the mean (SEM). Mean velocity was calculated from 12 nuclei. Repeated-measures analysis of variance (ANOVA) was conducted separately for between- (black) and through-constriction (red) measurements to examine whether cell migration speed varied with the number of constrictions.

motion corresponding to cycles of wrinkling and smoothing over time (Fig. 2C and movie S3). The pauses in between spikes coincided with smoothing, followed by a rapid acceleration, similar to recent observations by others (*24*). The step-like motion is likely due to the narrowing cross-sectional area as the cell moves through the constriction, which would necessitate an increase in speed to maintain a constant cellular "mass flow" rate. The overall motion of the nucleus, despite the step-like behavior, appeared to occur at constant speed (evident from the near constant slope of the position versus time data; Fig. 2C) with no obvious effects of the periodic constrictions on the nuclear speed. We confirmed this by measuring the speed of nuclear motion as a function of channel position for many nuclei (Fig. 2D). Consistent with the step-like motion of the nucleus, the mean speed of nuclei followed a saw-tooth pattern, with maximum and minimum speeds almost constant across the repeating constrictions. Repeated-measures analysis of variance (ANOVA), performed separately for between- and through-constriction measurements, showed no significant variation in cell migration velocity with the number of constrictions ($P > 0.05$).

Sometimes, constriction led to the formation of a bleb (movie S4) whose size increased in successive constrictions, with a corresponding decrease in the nuclear cross section (fig. S3). Eventually, the nucleus appeared to collapse in cross section, losing its constant curvature free surfaces, indicative of an inability to sustain a nuclear pressure. Blebs occurred in 24 and 16% of nuclei for 2 μm–by–7 μm and 3 μm–by–7 μm constrictions, respectively. Thus, a buildup of tension in the smooth nuclear lamina in the constriction corresponded with an increase in nuclear pressure, which caused blebs in a fraction of cells.

We measured the nuclear volume and surface area of GFP-lamin A/C–expressing HT-1080 nuclei during cell migration using 3D z-stacks from high-resolution 3D laser scanning confocal fluorescence microscopy. Nuclear surface area and volume were nearly constant (to within 5%) as the round nucleus changed to an hourglass shape in the constriction and back upon exit (Fig. 3, A and B). We found similar results with a GFP-lamin A/C–expressing HEY ovarian cancer cell line—nuclear volume and area remained approximately constant during nuclear deformation through the constriction (Fig. 3, C and D). These findings are consistent with our previous measurements of constant nuclear volume as the nucleus flattens during cell spreading (*16*, *25*). Others have reported increased nuclear volume in microchannels (*26*), but in that study, the microchannels imposed continuous constriction on cells rather than the periodic constrictions used in our study.

To explain these observations, we calculated the geometry of the constricted nucleus using a computational model. We computed nuclear shapes with an algorithm that maximizes the nuclear volume for a given surface area for nuclei at the center of the constriction (Fig. 3E). The optimization was performed by triangulating the nuclear lamina and stepping the vertices in the direction down the gradient of the energy with respect to vertex positions. Computed shapes were uniquely determined by a single parameter, λ, which is proportional to the ratio of pressure to surface tension. A unique nuclear shape emerged for a given value of λ that maximized the volume–to–surface area ratio for a nucleus centered in the constriction. The computed nuclear shapes, which resembled nuclei in the experiments, had a characteristic hourglass shape, and the free surfaces of the calculated shapes, i.e., those not in contact with channel walls, had a constant mean curvature.

By varying λ, we calculated the relationship between surface area and volume for the limiting shapes and compared it with experimental measurements. The calculated area-volume (A-V) curve (solid line in Fig. 3F) represents the range of limiting shapes within the constriction where the nucleus is predicted to be under pressure and the lamina to be under tension. Data points that fall along this curve indicate just enough surface area for a given volume for the nucleus to pass through the constriction. Data points above the curve would indicate that the nucleus has surface area exceeding the minimum needed to pass through the constriction for the given volume.

The nuclear volume and surface area measurements from live imaging experiments (Fig. 3, A and B) in HT-1080 cells fell on or above the computed A-V curves (Fig. 3F). Each point represents the mean volume and area for a nucleus within the constriction over five time points. Time zero was when the nucleus was at the center of the constriction, and two frames before and after time zero, separated by 2 min, were included in volume and area measurements for each nucleus. A comparison of the A-V experimental data with the model prediction suggests that the constrictions selected for those cells that had a laminar surface area at or above the minimum required for a given nucleus to fit into the constriction, without requiring volume compression or expansion of the laminar area (Fig. 3, A to F).

We also determined A-V curves for the HEY ovarian cancer cell line and mouse embryonic fibroblasts (MEFs) in channels of varying widths (Fig. 4A). For nuclei in fixed and DAPI–stained cells across cross-sectional areas of 2 μm by 7 μm, 3 μm by 7 μm, and 8 μm by 7 μm, the data were near or above the computationally predicted A-V curves, within experimental error. This suggests that when nuclei lacked sufficient excess area, i.e., the surface area above the area of a sphere of the same volume (see Eqs. 4 and 5 in Materials and Methods), they could not enter the constrictions. In addition, the A-V curve was shifted along the y axis in constrictions with narrower widths, again consistent with a selection mechanism (Fig. 4A). The excess surface area of the nuclear lamina, computed from the area and volume measurements, was higher in nuclei in constrictions with smaller widths than in constrictions with larger widths (Fig. 4B). Overall, the data are consistent with selection for nuclei with sufficient excess area in narrow constrictions.

We used the area minimization calculation to compute a volume-dependent minimum threshold excess area $\varepsilon_0(V)$ that a nucleus of a given volume V needed to pass through a constriction. Because lower values of excess area $\varepsilon < \varepsilon_0(V)$ are excluded, the model predicts that the overall frequency distribution of the excess areas of nuclei passing through the constrictions, $f(\varepsilon)$ will be shifted toward greater excess area. On the basis of the relationship $\varepsilon_0(V)$, $f(\varepsilon)$ was calculated as follows: We obtained the probability distributions of volumes $p(V)$ and fractional excess areas $p(\varepsilon)$ by fitting lognormal probability distributions to V and ε data for each cell type using the maximum likelihood estimation method (MATLAB's fitdist function). As we saw no correlation between V and ε, we assumed $p(\varepsilon)$ was independent of V. The predicted relative frequency $f(\varepsilon)$ of fractional excess areas of nuclei that could pass through the constriction was obtained by numerically integrating over the volume probability distribution while accounting for the threshold value $\varepsilon_0(V)$ for a given volume

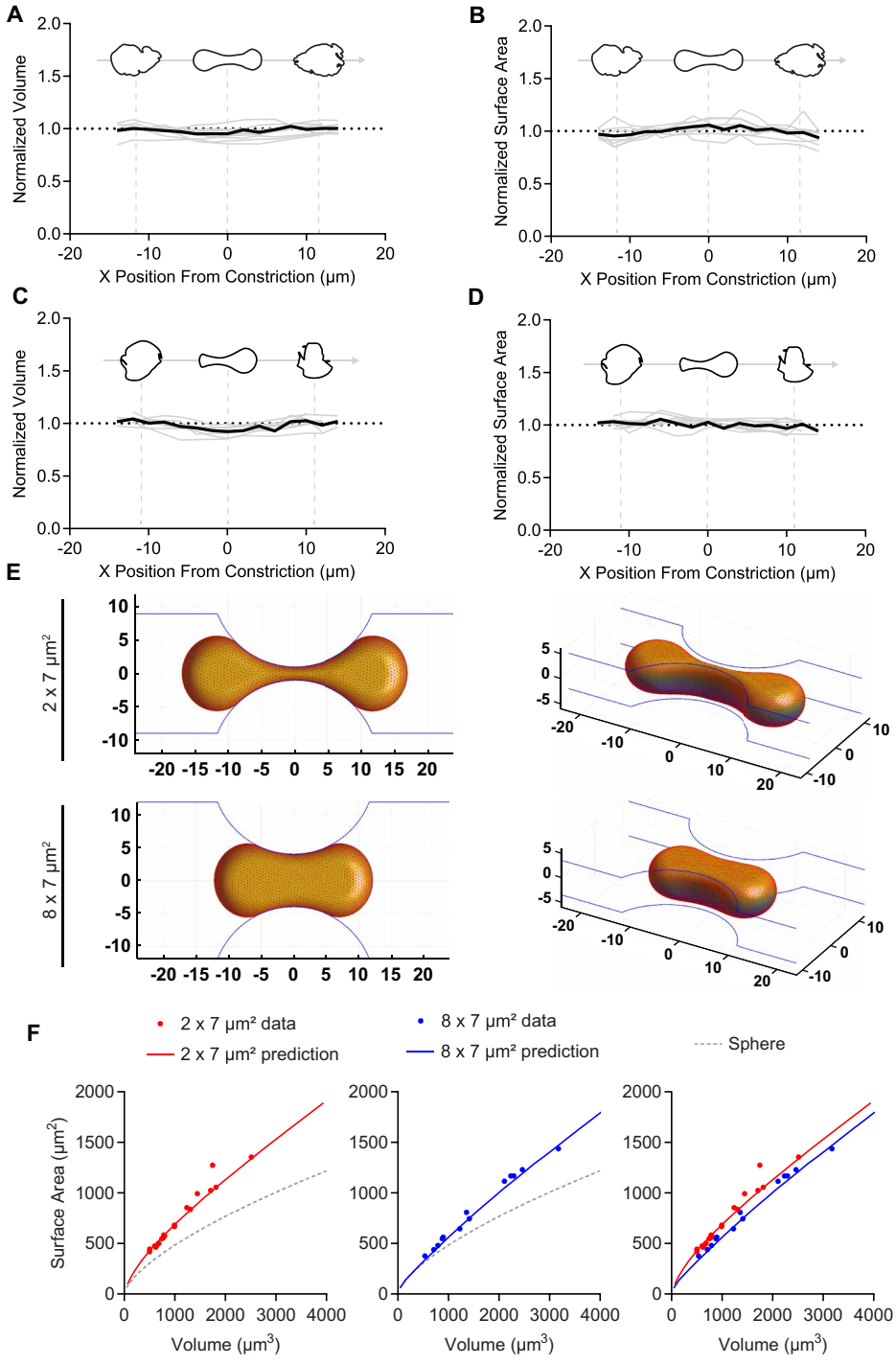

Fig. 3. Constrictions select for cells with a laminar area at or above a threshold value for a given volume. Normalized nuclear volume (**A**) and surface area (**B**) measured from 3D live imaging of HT-1080 nuclei expressing GFP-LMNA ($n = 9$) and volume (**C**) and (**D**) surface area of HEY nuclei expressing GFP-LMNA of ($n = 9$) as nuclei migrated through 2 μm–by–7 μm constrictions. Data are from two biological replicates. Illustrative nuclear shapes at different x positions are shown in the plot. (**E**) Examples of calculated nuclear shapes obtained from the computational model that maximized volume for a given surface area (axes units are in micrometer). Examples are shown with nuclear volumes of 1335 and 1352 μm^3 for 2 μm–by–7 μm and 8 μm–by–7 μm constrictions, respectively. The free surfaces that did not contact the channel walls have a constant mean curvature. (**F**) Nuclear surface area is plotted versus volume for nuclear shapes in 2 μm–by–7 μm (red) or 8 μm–by–7 μm (blue) constrictions. The solid curve represents the minimum area for a given volume (or maximum volume for a given area) of the nucleus required to occupy the center of the constriction, as determined by the optimization algorithm in (E). The dotted gray line represents the surface area of a sphere of the same volume. Experimental data that fell on the solid curve were assumed to be at the limiting shape. Points above the solid line show instances where the nucleus had the excess surface area needed to pass through the constriction without pressurizing the nucleus. $n = 19$ and 19 for 2 μm–by–7 μm and 8 μm–by–7 μm constrictions, respectively. Data are from three technical replicates for each of two biological replicates.

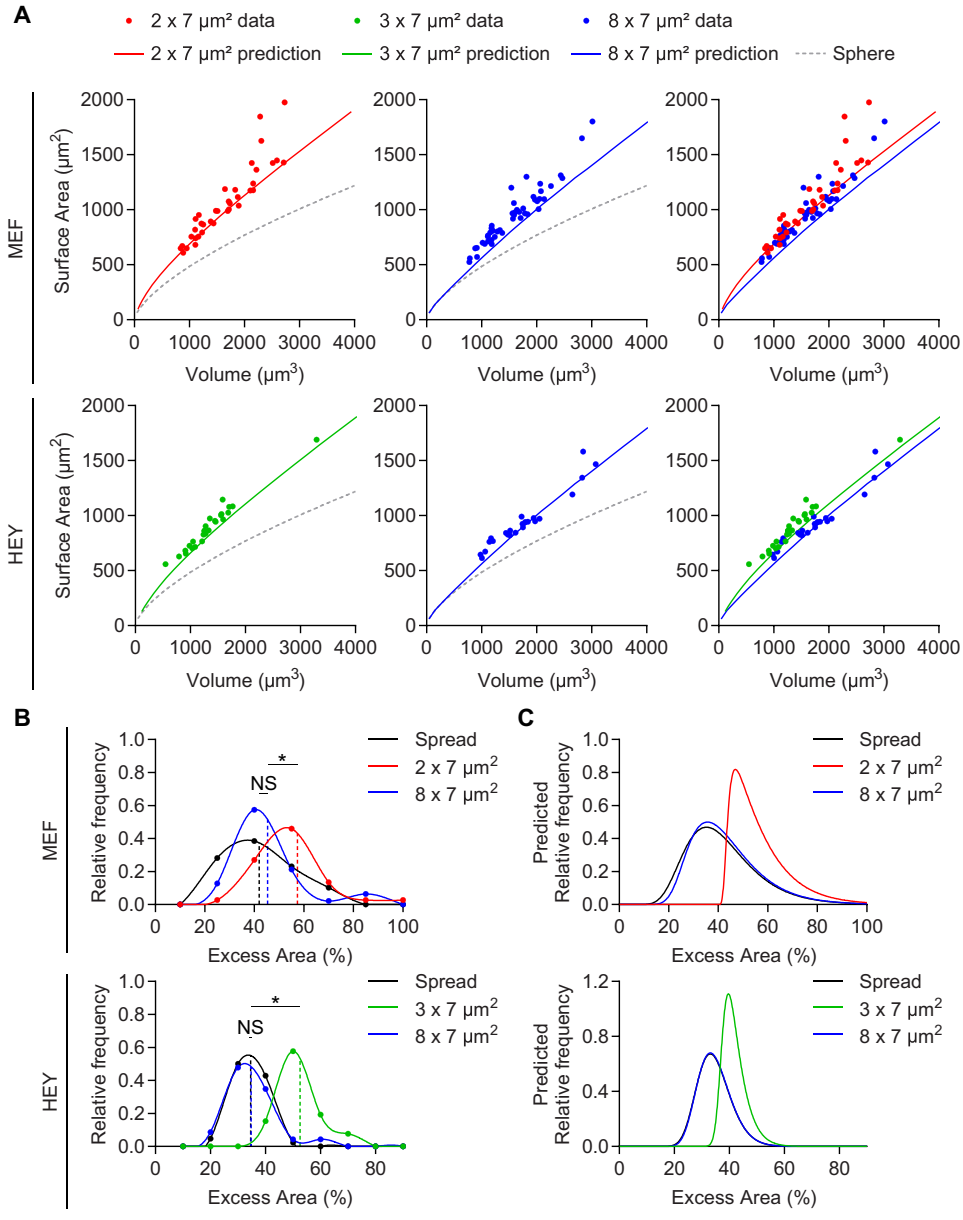

Fig. 4. Excess area distributions shift to higher values in confinement. (**A**) Nuclear surface area is plotted versus volume for limiting nuclear shapes confined to channel constriction. The solid curve represents the minimum area for a given volume (or maximum volume for a given area) of the nucleus to occupy the center of the constriction. The dotted gray line represents the surface area of a sphere of the same volume. The data points were measured for MEFs (top) or HEY cells (bottom) within the 2 μm–by–7 μm (red), 3 μm–by–7 μm (green), or 8 μm–by–7 μm (blue) constrictions. Points that fell on the solid curve are assumed to be at the limiting shape. Points above the solid line show instances where the nucleus had the excess surface area needed to pass through the constriction without pressurizing the nucleus. (**B**) Frequency distribution of excess area in MEFs or HEY cells in spread culture or within constrictions. n = 39, 37, 47, 42, 26, and 23 for spread MEFs, MEFs in 2 μm–by–7 μm, MEFs in 8 μm–by–7 μm, spread HEY cells, HEY cells in 3 μm–by–7 μm, and HEY cells in 8 μm–by–7 μm, respectively. Data are from three technical replicates for each of two biological replicates. Statistically significant differences between mean excess area (dashed line) were determined by one-way ANOVA, *$P < 0.05$; nonsignificant (NS): $P > 0.05$. (**C**) Predicted frequency distribution of excess area in MEFs or HEY cells in spread culture or within the constrictions.

$$f(\varepsilon) = \frac{\int_0^\infty p(V)p(\varepsilon)\mathscr{H}[\varepsilon - \varepsilon_0(V)]dV}{\int_0^\infty \int_0^\infty p(V)p(\varepsilon')\mathscr{H}[\varepsilon' - \varepsilon_0(V)]dVd\varepsilon'} \quad (1)$$

Here, $\mathscr{H}(x)$ is the Heaviside step function, $\mathscr{H}(x) \equiv \begin{cases} 0 \text{ for } x < 1 \\ 1 \text{ for } x \geq 1 \end{cases}$, which accounts for the assumption that nuclei of a given volume can pass through the constriction only when $\varepsilon \geq \varepsilon_0(V)$. The denominator ensures the integral of $f(\varepsilon)$ over all ε is equal to one. The resulting frequencies $f(\varepsilon)$ are shown in Fig. 4C for different channel sizes and cell types for comparison to experimental distributions in Fig.

4B. The computation reveals a rightward shift in the excess area frequencies in narrower constrictions similar to the experimental measurements. These experimental and computational results collectively show that nuclear passage through constriction depended on the amount of excess area in the lamina. Nuclei with insufficient excess area are excluded from constrictions because once the nuclear lamina becomes taut, further deformation is not possible owing to the inextensibility of the lamina.

To determine the role of lamin A/C, which primarily confers surface tension on the nucleus (*21*), we compared the shapes of the nuclear lamina in constrictions for mutant MEFs lacking the *LMNA* gene that encodes lamin A/C ($LMNA^{-/-}$ MEFs) (*27*) by staining lamin B1 (Fig. 5A). Like wild-type (WT) HT-1080 cells, free lamin B1–stained surfaces in WT MEF nuclei were smooth and curved. In contrast, in the mutant MEFs lacking lamin A/C, lamin B1 stained-free surfaces were highly irregular, indicating a failure to unfold the lamina and sustain a tension. Similar results were obtained upon depletion of lamin A/C with small interfering RNA (siRNA) transfection in HEY cells (Fig. 5A and fig. S4). To determine whether lamin A/C limits migration in constricting channels (*28*), we quantified the migration of cells through the periodic constrictions by measuring the surface density of cells that had exited the channel relative to the density of cells before entry (fig. S5). Consistent with prior observations (*10*), there were fewer WT MEFs (with lamin A/C) that had transited the channel compared with $LMNA^{-/-}$ MEFs lacking lamin A/C; likewise there were fewer control HEY cells that transited the channel compared with lamin A/C–depleted HEY cells (Fig. 5B).

The excess area hypothesis predicts that $LMNA^{-/-}$ MEFs, lacking lamin A/C, or HEY cells depleted of lamin A/C, migrate through constriction because they have an extensible lamina and can stretch their surface area to fit through constricting channels. We found that the *A*-*V* curves for both $LMNA^{-/-}$ MEFs and lamin A/C–depleted HEY cells were shifted above the computationally predicted curve (Fig. 5C), and the excess area was significantly greater in $LMNA^{-/-}$ MEFs compared to WT MEFs and in lamin A/C–depleted HEY cells compared to control HEY cells (Fig. 5, D and E). These results suggest that the inextensible lamin A/C–containing lamina that lacks sufficient excess area prevents entry of cells into the constriction. The lamina stretched freely in the absence of lamin A/C, allowing nuclei to fit into constrictions, which explains why more cells transited the channel in the absence of lamin A/C. Speed did not account for the difference in migration, as we found no significant differences in cell speed between $LMNA^{-/-}$ and WT MEFs (fig. S6).

DISCUSSION

The nucleus limits migration through narrow constrictions (*3*, *29*, *30*). Lower levels of lamin A/C correlate with higher migration through constrictions (*10*, *31*, *32*). Our data show that the nuclear lamina underwent repeated cycles of wrinkling and unwrinkling as the cell moved between wider and narrower regions, respectively. The passage of the cell through constrictions occurred at nearly constant nuclear surface area and volume. Experimental measurements and computational calculations of the surface area and the volume of nuclei revealed that constrictions selected for nuclei with surface areas above a threshold for a given volume (green area in Fig. 6A). These results are consistent with the threshold behavior predicted by the nuclear drop model, in which the flattening of round nuclei in culture requires folds/wrinkles in the lamina, and a fully taut and stiff lamina resists any further deformation of the nucleus, resulting in the limiting shapes of deformed nuclei with a taut lamina in spread cells (*16*, *19*). That is, nuclei with insufficient excess area in the lamina are excluded from constrictions because they cannot deform sufficiently to fit in them owing to the inextensibility of the taut lamina (yellow region in Fig. 6A and schematic in Fig. 6B).

In contrast to WT cells, cells lacking lamin A/C exhibited nuclei with highly irregular shapes in the constrictions. $LMNA^{-/-}$ MEF nuclei or lamin A/C–depleted HEY cells within the constriction lacked constant curvature surfaces, indicating a failure of the nucleus to generate surface tension in the lamin B1 nuclear lamina. These shapes suggest that the lamina can stretch without an apparent limit in the absence of lamin A/C. As a result, cells are not excluded from the constrictions even if they lack sufficient excess area to begin with (such a transition is indicated by vertical dashed arrow in Fig. 6A). This explains why larger numbers of cells are observed on the right side of the channels in the absence of lamin A/C or upon depletion of lamin A/C compared with control cells—fewer cells (if any) are excluded from entering the channels compared to control cells.

The ability of the computational model to predict the observed nuclear shapes indicates that the shapes of most nuclei in the constrictions are likely determined by the limited surface area of the nuclear lamina. If the surface area of the lamina is inextensible, then the calculated shapes of the nuclei represent the minimum volume compression needed for a given nuclear surface area. As changes in volume were not observed, nuclei must have sufficient laminar surface area to allow passage without significant compression of the nuclear volume. Nuclei that have more than this minimum area will pass easily through the constriction without reaching a limiting shape with a taut nuclear lamina. However, nuclei with area less than this minimum surface area must either decrease their volume sufficiently by compression or blebbing or rupture their nuclear envelope to pass through the constriction. Rupture or blebbing reduces the volume of the nucleus, allowing cells to transit through the constriction (transition indicated by horizontal, dashed arrow in Fig. 6A). Thus, geometric constraints on volume and surface area are sufficient to explain the hourglass nuclear shapes.

We also asked whether nuclear size limited the migration of cancer cells whose nuclei have sufficient excess area to pass through the constrictions. Neither the mean waiting time between successive constrictions nor the mean velocity through constrictions depended on the maximum cross-sectional area of the nucleus, a measure of nuclear size (fig. S7, A and B). Thus, size does not appear to be a major determinant of migration through constriction for the nuclei in a typical cell population, provided that the nuclei have sufficient excess area to fit through the constriction.

Typical interstitial tissue pore sizes range from 0.1 to 30 μm in diameter (*33*). Nuclei with sufficient excess surface area can theoretically fit within even the narrowest of constrictions without requiring any volume compression or surface area expansion, provided the constriction is short enough. We note that a shape consisting of two spheres conjoined at a point has only 26% more surface area than that of a single larger sphere of the same total enclosed volume. That is, a body with at least 26% excess surface area could geometrically deform to pass through a point constriction without any change of volume or surface area. Consistent with this, we have previously observed nuclei deforming like a drop to fit through extremely narrow pores formed by collagen fibers (*21*). Although a pore size of less than 10% of the nuclear cross section has been reported to

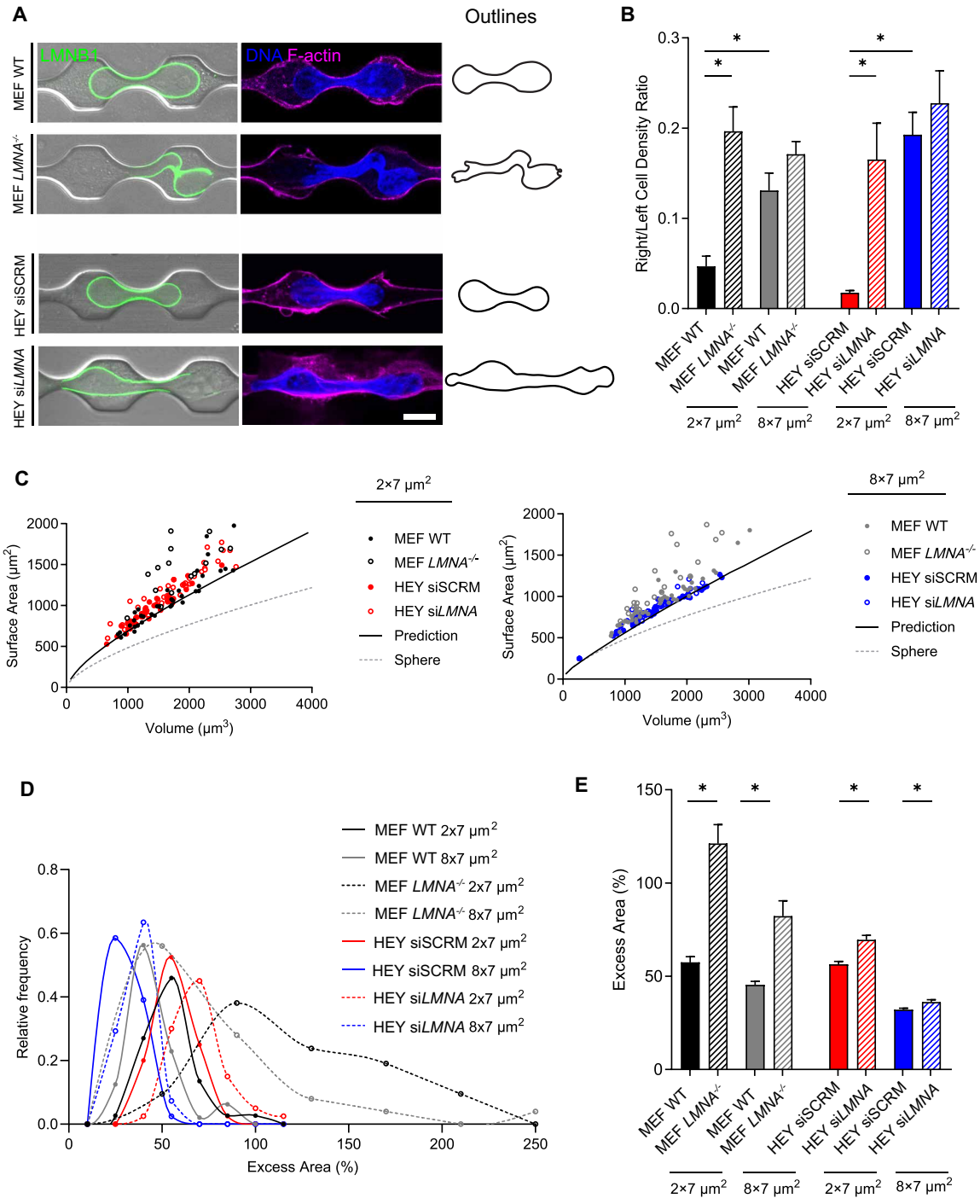

Fig. 5. Excess area of the lamin A/C–containing nuclear lamina limits migration in confinement. (**A**) Confocal images of lamin B1 (green), DNA (blue), and F-actin (magenta) staining are shown for WT versus *LMNA*$^{-/-}$ MEFs and siSCRM versus si*LMNA* HEY cells migrating through 2 μm–by–7 μm constrictions. Nuclear outlines delineated from DNA staining are shown on the right. Scale bar, 10 μm. (**B**) Right/left cell density ratios for WT and *LMNA*$^{-/-}$ MEFs as well as siSCRM and si*LMNA* HEY cells were quantified after a 36-hour migration in 2 μm–by–7 μm and 8 μm–by–7 μm constrictions. Error bars, SEM. Mean ratio was calculated based on three biological replicates. *$P < 0.05$ by an unpaired *t* test. (**C**) Nuclear surface area is plotted versus nuclear volume for cells confined to channel constriction. The solid curve represents the minimum area for a given volume (or maximum volume for a given area) of the nucleus required to occupy the center of the constriction. The dotted gray line represents the surface area of a sphere of the same volume. The data points are measured for WT MEFs or HEY cells transfected with scrambled siRNA (siSCRM, solid circles) and *LMNA*$^{-/-}$ MEFs or HEY cells transfected with siRNA toward *LMNA* (si*LMNA*, open circles) within a 2 μm–by–7 μm (black and red, respectively) or 8 μm–by–7 μm (gray and blue, respectively) constriction. (**D**) Frequency distribution and (**E**) mean values of the excess area in WT or *LMNA*$^{-/-}$ MEFs and siSCRM or si*LMNA* HEY cells within 2 μm–by–7 μm or 8 μm–by–7 μm constrictions. $n = 37$, 21, 47, and 25 for the four MEF groups and $n = 40$, 40, 40, 40 for HEY groups shown on the *x* axis in (E). Error bars, SEM. *$P < 0.05$ by unpaired *t* test. Data are from four technical replicates for each of two biological replicates for each condition.

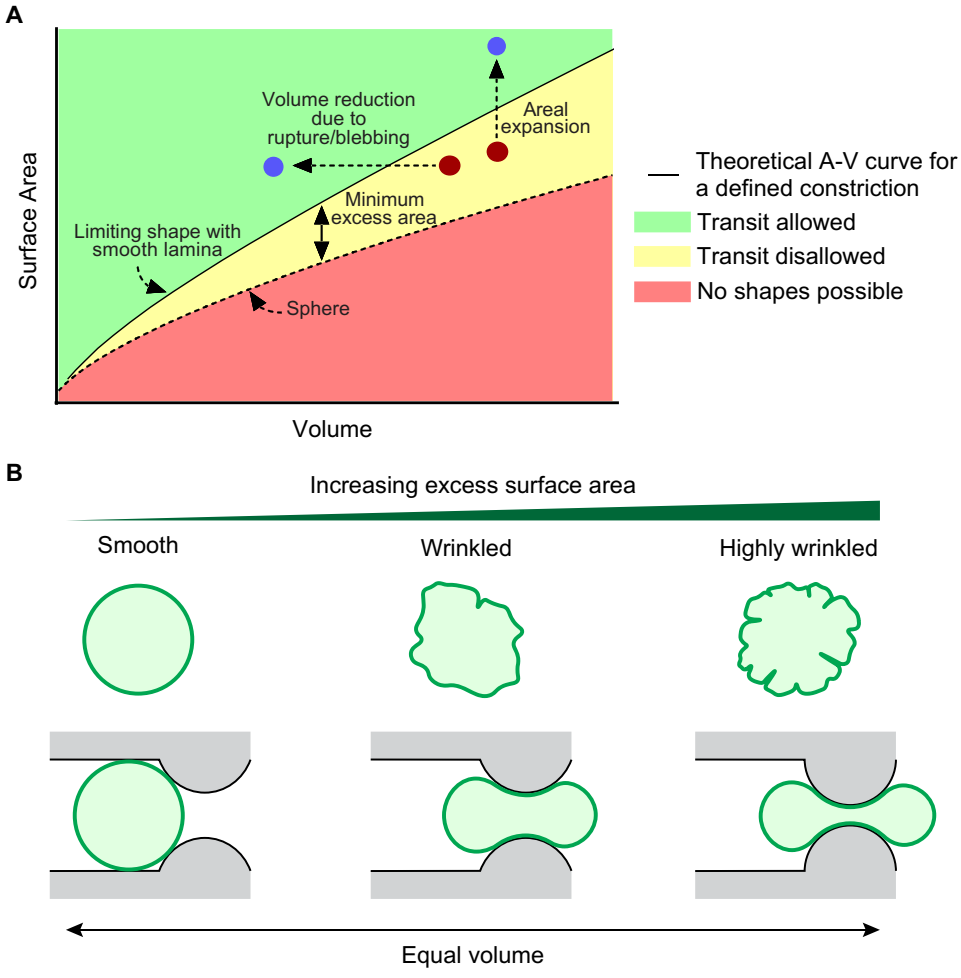

Fig. 6. The constrictions select for the cells that had a sufficient surface area of lamina to fit into the constriction. (**A**) Schematic diagram that depicts the role of excess laminar surface area in confining migration. The surface area volume curve (solid black line) depicts the minimum surface area for a given volume required to pass through a given specific constriction geometry (i.e., a constriction with a defined shape and dimensions) without a change in volume or surface area. Nuclei with laminar surface area in excess of the minimum surface area (green region) will be able to transit through the constrictions (green region). Nuclei with area less than the minimum surface area will be unable to transit (yellow region). Areal expansion at constant volume, which can only occur in the absence of lamin A/C, or volume reduction due to rupture/blebbing will allow cells to transit through even if they started in the yellow region. The dashed curve represents the area-volume curve for a sphere, below which no shapes are geometrically possible (red region). (**B**) Schematic diagram shows that the nuclei with insufficient excess area in the lamina were excluded from constrictions due to inadequate deformability (left). The nuclei with sufficient excess surface area were allowed to pass through the constriction with their laminar wrinkles smoothing out (middle), and the nuclei with greater excess area were selected for passage through constrictions of smaller widths (right).

limit cell migration (*3*), our results suggest that the overall shape of the constriction (i.e., length as well as width) will determine the minimum surface area required for the nucleus to transit through the pore without requiring nuclear volume compression or laminar area expansion.

The reported viscoelasticity of the nucleus is based on mechanical measurements performed over a time scale of several seconds [for example, (*34*)]. However, a typical 12- to 15-μm nucleus migrates through the constriction at about 3 μm/min (Fig. 2D), deforming over the 4 to 5 min of passage through the constriction. On this longer timescale with slow deformation rates, the storage of elastic energy in the chromatin is expected to have dissipated (*22*). This may explain why laminar surface tension dominates resistance to nuclear deformation over the timescale of cell migration.

Drop-like nuclear deformation with the surface tension imposed by the nuclear lamina appears to occur through narrow spaces created by fibrous obstacles (*21*) and constricting channels as reported here. However, the surface tension imparted by lamin A/C has opposing effects. During confining migration through fibrous obstacles, lamin A/C allows indentations to occur while maintaining overall nuclear drop integrity and preventing entanglement of the nucleus around obstacles (*21*). In contrast, during migration through confining environments, lamin A/C unwrinkling hinders migration owing to a buildup of surface tension during confinement.

MATERIALS AND METHODS

Cell culture

Cells were maintained in a humidified incubator at 37°C with 5% CO_2. HT-1080 human fibrosarcoma cells [CCL121, American Type Culture Collection (ATCC), Manassas, VI] and HEY human ovarian cancer cells (305017, Cell Lines Service, Sioux Falls, SD) were cultured

in Dulbecco's modified Eagle's medium (DMEM) with glucose (4.5 g liter^{-1}; 10-013-CV, Corning, Corning, NY) supplemented with 10% (v/v) fetal bovine serum (16140071, Thermo Fisher Scientific, Waltham, MA) and 1% (v/v) penicillin/streptomycin (30-002-CI, Corning, Corning, NY). WT MEFs and *LMNA*$^{-/-}$ MEFs (a kind gift from the K. Roux laboratory) were cultured in DMEM with glucose (4.5 g liter^{-1}; 10-013-CV, Corning, Corning, NY) supplemented with 15% (v/v) fetal bovine serum (16140071, Thermo Fisher Scientific, Waltham, MA) and 1% Roux penicillin/streptomycin (30-002-CI, Corning, Corning, NY).

Plasmid and stable cell line generation

The pBABE-puro-GFP-wt-lamin A plasmid was purchased from Addgene (plasmid #17662) (*35*). The pBABE-puro-GFP-BAF plasmid was a gift from K. Roux (*36*). GFP fusion genes were stably expressed in HT-1080 cells by retroviral transduction. To prepare viral particles, Phoenix-Ampho cells were transfected with pBabe plasmid DNA using Lipofectamine 3000 (Thermo Fisher Scientific, Waltham, MA) according to the manufacturer's protocol. Transfected Phoenix-Ampho cells were incubated at 37°C for 8 hours, provided with fresh culture medium, and maintained at 32°C for 48 hours. The culture medium containing packaged retrovirus was collected and filtered through 0.45-μm filters (Thermo Fisher Scientific, Waltham, MA). Filtered medium supplemented with polybrene (2.5 μg ml^{-1}; Sigma-Aldrich, Saint Louis, MO) was added to the target HT-1080 cells. The target cells were incubated at 37°C for 48 hours and then provided with fresh culture medium containing puromycin (Sigma-Aldrich, Saint Louis, MO) for selection of viral integration. After 2 to 3 days of antibiotic selection, the expression of the GFP fusion protein in HT-1080 cells was verified using immunofluorescence and immunoblot analyses.

Transfection of siRNAs

HEY WT cells were cultured in 25-cm^2 culture flasks in an antibiotic-free medium for 40% confluency at the time of transfection. The transfection solution of 0.25% Lipofectamine RNAiMAX transfection reagent (Invitrogen) and 0.4% siRNA (Dharmacon, siGENOME Non-Targeting Control siRNA Pool #2, D-001206-14-05, target sequences: UAAGGCUAUGAAGAGAUAC, AUGUAUUGGCCUGUAUUAG, AUGAACGUGAAUUGCUCAA, UGGUUUACAUGUCGACUAA; *LMNA* siGENOME SMARTpool siRNA, D004978-01, target sequence: GAAGGAGGGUGACCUGAUA) in the reduced serum Opti-MEM medium (Gibco) were added to the flasks after removing the medium. After 48 hours of incubation in the incubator, cells were collected for polymerase chain reaction (PCR) assay to verify RNA knockdown efficiency and passing on the confining migration devices.

Reverse transcriptase quantitative PCR

To determine the efficiency of knockdown, cells were harvested and lysed using the RNeasy Plus Kit (QIAGEN), and RNA was purified and quantified. The cDNA was prepared by mixing RNA, reverse transcriptase, oligo primers, and nucleotide triphosphates (dNTPs) (iScript Advanced cDNA Synthesis Kit, Bio-Rad Laboratories) in PCR-grade nuclease-free water (Invitrogen) and incubation at the appropriate temperature and duration for reverse transcription (Bio-Rad thermocycler). Forward and reverse primer sets [*GAPDH*: VHPS-3541, forward (5′-3′): GAGTCAACGGATTTGGTCGT, reverse (5′-3′): TTGATTTTGGAGGGATCTCG, RealTimePrimers; *LMNA*: Ref# 460260112 460260113, forward sequence: ATGAGGACCAGGTGGAGCAGTA; reverse sequence: ACCAGGTTGCTGTTCCTC-TCAG] were used to target the cDNA of the genes of interest. The PCR reaction combined cDNA, primers, DNA polymerase, dNTPs, and iQ SYBR Green Supermix reaction buffer (Bio-Rad Laboratories). PCR amplification was performed using appropriate cycling conditions recommended by Bio-Rad. The standard curves and Cycle threshold (Ct) values were used to quantify gene expression levels for the genes of interest normalized to the expression level of *GAPDH* in the treatment group relative to the normalized gene expression levels in the siScramble RNA (siSCRM) group.

Fluorescent staining

For imaging lamin B1, DNA, or F-actin in fixed samples, cells were treated with 4% paraformaldehyde (15710, Electron Microscopy Sciences, Hatfield, PA) for 20 min at room temperature, permeabilized with 0.1% Triton X-100 (85111, Thermo Fisher Scientific, Waltham, MA) in phosphate-buffered saline (PBS) (21-040-CM, Corning, Corning, NY), and blocked with bovine serum albumin (1 mg ml^{-1}; BP9703100, Thermo Fisher Scientific) for 1 hour at room temperature. Cells were incubated with primary antibody rabbit anti-lamin B1 (dilution, 1:1000; ab229025, Abcam, Waltham, MA) overnight at 4°C. The cells were then washed with PBS and incubated with secondary antibody Alexa Fluor 488 goat anti-rabbit (dilution, 1:200; A11034, Thermo Fisher Scientific, Waltham, MA) for 2 hours at room temperature. Hoechst 33342 (dilution, 1:1000; 875756-97-1, Sigma-Aldrich, Saint Louis, MO) was used to stain DNA, and Alexa Fluor 647 Phalloidin (dilution, 1:1000; A22287, Thermo Fisher Scientific, Waltham, MA) was used to stain F-actin.

Imaging

Confocal imaging was performed on a Zeiss LSM 900 microscope (Carl Zeiss Jena GmbH, Jena, Germany) using a C Plan-Apochromat 63×/1.4 oil objective (421782-9900-000, Carl Zeiss Jena GmbH, Jena, Germany) or an Olympus FV3000 confocal microscope using a 60×/1.3 NA silicone oil-immersion objective(Olympus Scientific Solutions Americas Corp.). The 3D imaging of fixed and live samples with Zeiss microscope was done using a pinhole opening of one Airy disk and a *z*-step size of 230 nm to ensure overlapping z-stacks, with sampling at less than half of the depth of focus (corresponding to an optical section of ≈500 nm for 488 nm light) to satisfy Nyquist criterion and minimize photobleaching artifacts (*37*). Imaging of live and fixed samples on Olympus microscope was done with 230-nm and 130-nm z-step sizes, respectively. Live 2D and 3D imaging was done in a temperature- and humidity-controlled chamber (PeCon GmbH, Erbach, Germany) at 37°C with 5% CO_2. The imaging of fixed samples for cell transit analysis was performed on an ECHO Revolve R4 (ECHO, San Diego, CA) using a N Plan-Apochromat 2×/0.08 objective (N1480200, Olympus Scientific Solutions Americas Corp., Waltham, MA).

Wafer fabrication

The confined migration devices were designed in AutoCAD 2018. The platform was fabricated in PDMS using a two-step photolithography master mold fabrication process, followed by a soft lithography replica molding process to construct the final PDMS device from the master mold. First, the AutoCAD design was patterned on a chrome-coated glass mask using a Heidelberg DWL66+ Laser Pattern Generator. Second, to create the master mold for layer one, a

layer of photosensitive epoxy (SU-8; Kayaku, USA) was patterned on a 3-inch diameter silicon substrate [3″ N/Ph (1-0-0) 10–20 ohm-cm, 381 ± 25μm PRIME SILICON WAFER, SSP, 2 SEMI FLATS] by spin coating SU-8 2007 (Microchem, Westborough, MA) at 2100 rpm for 30 s and soft baking at 95°C for 3 min to obtain a 7-μm layer thickness. This unit was exposed to ultraviolet (UV) light using photolithography (EVG 610 Double-Slide Mask Aligner) at an exposure energy equal to 130 mJ/cm^2 through a photomask, followed by a post-exposure bake at 95°C for 5 min. The master mold for layer two was fabricated by spin coating SU-8 2035 (Microchem, Westborough, MA) at 1300 rpm for 30 s and soft baking at 55°C for 30 min, 95°C for 45 min, and then at 55°C overnight to obtain a 200-μm layer thickness. This unit was exposed to UV light using photolithography (EVG 610 Double-Slide Mask Aligner) at an exposure energy equal to 325 mJ/cm^2 through a photomask, followed by a post-exposure bake at 95°C for 5 min. Then, the wafers were developed using an SU-8 developer (Microchem, Westborough, MA). Both master molds were coated with (tridecafluoro1,1,2,2-tetrahydro octyl) trichlorosilane (T2492, United Chemical Technologies Inc., Bristol, PA) (≈50 nm thick using Chemical Vapor Deposition) for 30 min to facilitate PDMS release from the master mold after replication.

Soft lithography

A negative mold was prepared from a patterned master silicon wafer using PDMS (Sylgard 184, Dow Corning, Midland, MI) mixed at the base at a cross-linking agent ratio of 10:1 (w/w) and cured at 60°C for 2 hours. After curing, the negative was peeled carefully from the wafer and cut into blocks following the pattern. Each block was cut to fit in a no. 1.5 glass-bottom dish (FD35-100, WPI Inc., Sarasota County, FL), and 5- and 1-mm holes were punched using biopsy punches as media reservoirs and cell seeding inlets, respectively. Then, the PDMS blocks and the glass-bottom dishes were treated with plasma (Harrick Plasma, Ithaca, NY) for 90 s. Following plasma treatment, the PDMS blocks were pressed pattern-side down onto the glass-bottom dishes and placed on a hot plate at 85°C for at least 15 min to form a covalent bond between the PDMS and the glass.

Device preparation and cell seeding

Devices were passivated with anhydrous 200-proof ethanol, washed three times with PBS, and incubated at room temperature for 30 min to remove traces of ethanol. Then, the migration channel was filled with fibronectin (50 μg ml$^{-1;}$ 356008, Corning, Corning, NY) in PBS and incubated for at least 2 hours at 37°C. Following incubation, cells were trypsinized (Corning, Corning, NY), counted, and resuspended in a complete medium. The devices were washed twice with a complete cell medium, and approximately 50,000 cells were seeded into each of the left 1-mm inlets in 5-μl aliquots and left to attach overnight before we changed the medium. The medium was changed in both 5-mm reservoirs simultaneously, each with a 100-μl aliquot. The aliquot in the right 5-mm reservoir contained platelet-derived growth factor (PDGF) (200 ng ml^{-1}; 220-BB, R&D Systems, Minneapolis, MN) to provide a stable growth factor gradient. The medium was changed, and the gradient was re-established after approximately 18 hours.

Computation of nuclear shapes

Nuclear shapes were computed by minimizing the energy associated with stretching the surface area and compressing the volume. The nuclear surface as segmented into 6088 linear triangular elements, and triangle energies were calculated from an energy function associated with the Voronoi cells $\{v_i\}$ around each vertex $\{x_i\}$ (3046 total). To maintain a centroidal Voronoi tessellation, the energy of the Voronoi cells is given by

$$E(\{x_i\}) = N\sum_{i=1}^{N}\int_{y\in v_i\subset\mathcal{M}(X)}\|y-x_i\|^2 d\sigma(y) \quad (2)$$

which is asymptotically proportional to the square of the surface of the triangular mesh, following the algorithm of Pan *et al.* (*38*). The total energy, including that of the volume, is

$$E_{\text{tot}}(\{x_i\}) = E(\{x_i\}) + \lambda V(\{x_i\}) \quad (3)$$

where λ is the parameter that determines the size of the triangular mesh surface. Vertex positions were iteratively advanced opposite the direction of the energy gradient with respect to $\{x_i\}$; i.e., $-\nabla E_{\text{tot}}(\{x_i\})$ toward an energy minimum. Any vertices that stepped over the channel surfaces during an iteration were corrected by projecting the vertex position back onto the nearest channel surface. Minimizing the energy for a given λ yielded a unique nuclear shape with surfaces of constant mean curvature (where not in contact with the channel walls). To prevent the nucleus from moving away from the center of the constriction, we added an additional force to all vertices that was proportional to the distance of the mean vertex position from the channel center. Therefore, the final shape from the algorithm was the energy minimum under the constraint of the nucleus being centered in the constriction. Therefore, the final shape resulting from algorithm was the energy minimum under the constraint of being centered in the constriction. For the narrow 2 μm–by–7 μm and 3 μm–by–7 μm channels with larger nuclear volumes (above about 250 μm^3 and 1700 μm^3, respectively), the region of the nucleus in the channel would continue to thin as the algorithm approached an energy minimum with nucleus pinched off into two subregions divided by the channel. This outcome was not observed and considered to be physically unrealizable during the time course of nucleus passing through the channel, so an additional constraint was added to maintain wall contact of the nucleus at the top, bottom, and sides of the channel. This was achieved by preventing the nucleus from narrowing past a 5-μm–long horizontal elliptical cylinder centered in the constriction with the lateral and vertical dimensions of the channel (2- or 3-μm wide by 7-μm height).

Image analysis

Raw confocal images were loaded into MATLAB, and a customized MATLAB code was built to analyze nuclear morphometry and cell migration. Images of the lamin or DNA staining were segmented using an Otsu segmentation algorithm to generate nuclear masks. The maximum and minimum x positions of the nuclear mask were measured as front and trailing edge positions, respectively. The centroid position was measured using the MATLAB Image Processing Toolbox. To measure the wrinkling index from lamin images, we generated a periphery mask through morphological thinning of the nuclear mask with an empirically determined width. The pixels in the lamin segmentation covered by the periphery mask were excluded, and the remaining pixels inside were identified as wrinkling pixels. The wrinkling index was calculated as the area of the wrinkling pixels divided by the area of the nuclear mask. To measure nuclear volume from 3D confocal images, z-stack lamin images were segmented using an Otsu segmentation algorithm in each z plane. Nuclear surface area

A and volume V were quantified using the MATLAB Image Processing Toolbox. Excess area ε was calculated by

$$\varepsilon = A / A_{\text{sphere}} - 1 \quad (4)$$

where A_{sphere} is the surface area of the sphere and is geometrically related to V by

$$A_{\text{sphere}} = (36\pi)^{1/3} V^{2/3} \quad (5)$$

To quantify cell density in the migration experiment, we segmented the DNA images using an Otsu segmentation algorithm to obtain nuclear masks. The channel region and its left and right regions were labeled manually. The cell density was calculated as the number of nuclei divided by the area of each region.

Statistical analysis

GraphPad Prism 10.0 was used for statistical analysis and graphic representations of data. Differences between values were considered statistically significant when $P < 0.05$ and nonsignificant for $P > 0.05$. The details of experimental conditions and statistical tests are provided in the figure legends.

Supplementary Materials

The PDF file includes:
Figs. S1 to S7
Legends for movies S1 to S4

Other Supplementary Material for this manuscript includes the following:
Movies S1 to S4

REFERENCES AND NOTES

1. T. Kitamura, B. Z. Qian, J. W. Pollard, Immune cell promotion of metastasis. *Nat. Rev. Immunol.* **15**, 73–86 (2015).
2. F. Qu, Q. Li, X. Wang, X. Cao, M. H. Zgonis, J. L. Esterhai, V. B. Shenoy, L. Han, R. L. Mauck, Maturation state and matrix microstructure regulate interstitial cell migration in dense connective tissues. *Sci. Rep.* **8**, 3295 (2018).
3. K. Wolf, M. Te Lindert, M. Krause, S. Alexander, J. Te Riet, A. L. Willis, R. M. Hoffman, C. G. Figdor, S. J. Weiss, P. Friedl, Physical limits of cell migration: Control by ECM space and nuclear deformation and tuning by proteolysis and traction force. *J. Cell Biol.* **201**, 1069–1084 (2013).
4. F. J. Calero-Cuenca, C. S. Janota, E. R. Gomes, Dealing with the nucleus during cell migration. *Curr. Opin. Cell Biol.* **50**, 35–41 (2018).
5. F. Hemmati, A. Akinpelu, J. Song, F. Amiri, A. McDaniel, C. McMurray, A. Afthinos, S. T. Andreadis, A. V. Aitken, V. C. Biancardi, Downregulation of YAP activity restricts P53 hyperactivation to promote cell survival in confinement. *Adv. Sci.* **10**, 2302228 (2023).
6. E. O. Wisniewski, P. Mistriotis, K. Bera, R. A. Law, J. Zhang, M. Nikolic, M. Weiger, M. Parlani, S. Tuntithavornwat, A. Afthinos, Dorsoventral polarity directs cell responses to migration track geometries. *Sci. Adv.* **6**, eaba6505 (2020).
7. T. Harada, J. Swift, J. Irianto, J.-W. Shin, K. R. Spinler, A. Athirasala, R. Diegmiller, P. D. P. Dingal, I. L. Ivanovska, D. E. Discher, Nuclear lamin stiffness is a barrier to 3D migration, but softness can limit survival. *J. Cell Biol.* **204**, 669–682 (2014).
8. Y. L. Dorland, A. S. Cornelissen, C. Kuijk, S. Tol, M. Hoogenboezem, J. D. van Buul, M. A. Nolte, C. Voermans, S. Huveneers, Nuclear shape, protrusive behaviour and in vivo retention of human bone marrow mesenchymal stromal cells is controlled by Lamin-A/C expression. *Sci. Rep.* **9**, 14401 (2019).
9. S.-J. Heo, K. H. Song, S. Thakur, L. M. Miller, X. Cao, A. P. Peredo, B. N. Seiber, F. Qu, T. P. Driscoll, V. B. Shenoy, M. Lakadamyali, J. A. Burdick, R. L. Mauck, Nuclear softening expedites interstitial cell migration in fibrous networks and dense connective tissues. *Sci. Adv.* **6**, eaax5083 (2020).
10. E. S. Bell, P. Shah, N. Zuela-Sopilniak, D. Kim, A. A. Varlet, J. L. P. Morival, A. L. McGregor, P. Isermann, P. M. Davidson, J. J. Elacqua, J. N. Lakins, L. Vahdat, V. M. Weaver, M. B. Smolka, P. N. Span, J. Lammerding, Low lamin A levels enhance confined cell migration and metastatic capacity in breast cancer. *Oncogene* **41**, 4211–4230 (2022).
11. X. Cao, E. Moeendarbary, P. Isermann, P. M. Davidson, X. Wang, M. B. Chen, A. K. Burkart, J. Lammerding, R. D. Kamm, V. B. Shenoy, A chemomechanical model for nuclear morphology and stresses during cell transendothelial migration. *Biophys. J.* **111**, 1541–1552 (2016).
12. F. Alisafaei, D. S. Jokhun, G. V. Shivashankar, V. B. Shenoy, Regulation of nuclear architecture, mechanics, and nucleocytoplasmic shuttling of epigenetic factors by cell geometric constraints. *Proc. Natl. Acad. Sci. U.S.A.* **116**, 13200–13209 (2019).
13. M. Versaevel, T. Grevesse, S. Gabriele, Spatial coordination between cell and nuclear shape within micropatterned endothelial cells. *Nat. Commun.* **3**, 671 (2012).
14. R. Vishavkarma, S. Raghavan, C. Kuyyamudi, A. Majumder, J. Dhawan, P. A. Pullarkat, Role of actin filaments in correlating nuclear shape and cell spreading. *PLOS ONE* **9**, e107895 (2014).
15. H.-P. Lee, F. Alisafaei, K. Adebawale, J. Chang, V. B. Shenoy, O. Chaudhuri, The nuclear piston activates mechanosensitive ion channels to generate cell migration paths in confining microenvironments. *Sci. Adv.* **7**, eabd4058 (2021).
16. T.-C. Wang, S. Abolghasemzade, B. P. McKee, I. Singh, K. Pendyala, M. Mohajeri, H. Patel, A. Shaji, A. L. Kersey, K. Harsh, S. Kaur, C. R. Dollahon, S. Chukkapalli, P. P. Lele, D. E. Conway, A. K. Gaharwar, R. B. Dickinson, T. P. Lele, Matrix stiffness drives drop like nuclear deformation and lamin A/C tension-dependent YAP nuclear localization. *Nat. Commun.* **15**, 10151 (2024).
17. B. D. Cosgrove, C. Loebel, T. P. Driscoll, T. K. Tsinman, E. N. Dai, S.-J. Heo, N. A. Dyment, J. A. Burdick, R. L. Mauck, Nuclear envelope wrinkling predicts mesenchymal progenitor cell mechano-response in 2D and 3D microenvironments. *Biomaterials* **270**, 120662 (2021).
18. R. B. Dickinson, A. Katiyar, C. R. Dubell, T. P. Lele, Viscous shaping of the compliant cell nucleus. *APL Bioeng.* **6**, 010901 (2022).
19. R. B. Dickinson, T. P. Lele, Nuclear shapes are geometrically determined by the excess surface area of the nuclear lamina. *Front. Cell Dev. Biol.* **11**, 1058727 (2023).
20. R. B. Dickinson, T. P. Lele, A new function for nuclear lamins: Providing surface tension to the nuclear drop. *Curr. Opin. Biomed. Eng.* **28**, 100483 (2023).
21. A. Katiyar, J. Zhang, J. D. Antani, Y. Yu, K. L. Scott, P. P. Lele, C. A. Reinhart-King, N. J. Sniadecki, K. J. Roux, R. B. Dickinson, T. P. Lele, The nucleus bypasses obstacles by deforming like a drop with surface tension mediated by lamin A/C. *Adv. Sci.* **9**, e2201248 (2022).
22. V. J. Tocco, Y. Li, K. G. Christopher, J. H. Matthews, V. Aggarwal, L. Paschall, H. Luesch, J. D. Licht, R. B. Dickinson, T. P. Lele, The nucleus is irreversibly shaped by motion of cell boundaries in cancer and non-cancer cells. *J. Cell. Physiol.* **233**, 1446–1454 (2018).
23. C. M. Denais, R. M. Gilbert, P. Isermann, A. L. McGregor, M. te Lindert, B. Weigelin, P. M. Davidson, P. Friedl, K. Wolf, J. Lammerding, Nuclear envelope rupture and repair during cancer cell migration. *Science* **352**, 353–358 (2016).
24. M. Geiger, P. Marsico, D. Pensold, M. Wessling, G. Zimmer-Bensch, J. Linkhorst, A microfluidic perfusion culture setup to investigate cell migration in 3D constrictions. *Adv. Mater. Technol.* **9**, 2301535 (2024).
25. Y. Li, D. Lovett, Q. Zhang, S. Neelam, R. A. Kuchibhotla, R. Zhu, G. G. Gundersen, T. P. Lele, R. B. Dickinson, Moving cell boundaries drive nuclear shaping during cell spreading. *Biophys. J.* **109**, 670–686 (2015).
26. P. Mistriotis, E. O. Wisniewski, K. Bera, J. Keys, Y. Li, S. Tuntithavornwat, R. A. Law, N. A. Perez-Gonzalez, E. Erdogmus, Y. Zhang, R. Zhao, S. X. Sun, P. Kalab, J. Lammerding, K. Konstantopoulos, Confinement hinders motility by inducing RhoA-mediated nuclear influx, volume expansion, and blebbing. *J. Cell Biol.* **218**, 4093–4111 (2019).
27. Y. Kim, Y. Zheng, Generation and characterization of a conditional deletion allele for Lmna in mice. *Biochem. Biophys. Res. Commun.* **440**, 8–13 (2013).
28. N. Alcorta-Sevillano, I. Macias, C. I. Rodriguez, A. Infante, Crucial role of lamin A/C in the migration and differentiation of MSCs in bone. *Cells* **9**, 1330 (2020).
29. L. R. Smith, J. Irianto, Y. Xia, C. R. Pfeifer, D. E. Discher, Constricted migration modulates stem cell differentiation. *Mol. Biol. Cell* **30**, 1985–1999 (2019).
30. S. Stöberl, J. Flommersfeld, M. M. Kreft, M. Benoit, C. P. Broedersz, J. O. Rädler, Nuclear deformation and dynamics of migrating cells in 3D confinement reveal adaptation of pulling and pushing forces. *Sci. Adv.* **10**, eadm9195 (2024).
31. H.-R. Thiam, P. Vargas, N. Carpi, C. L. Crespo, M. Raab, E. Terriac, M. C. King, J. Jacobelli, A. S. Alberts, T. Stradal, A. M. Lennon-Dumenil, M. Piel, Perinuclear Arp2/3-driven actin polymerization enables nuclear deformation to facilitate cell migration through complex environments. *Nat. Commun.* **7**, 10997 (2016).
32. L. Penfield, D. J. Montell, Nuclear lamin facilitates collective border cell invasion into confined spaces in vivo. *J. Cell Biol.* **222**, e202212101 (2023).
33. A. L. McGregor, C.-R. Hsia, J. Lammerding, Squish and squeeze-the nucleus as a physical barrier during migration in confined environments. *Curr. Opin. Cell Biol.* **40**, 32–40 (2016).
34. C. M. Hobson, M. Kern, E. T. O'Brien III, A. D. Stephens, M. R. Falvo, R. Superfine, Correlating nuclear morphology and external force with combined atomic force microscopy and light sheet imaging separates roles of chromatin and lamin A/C in nuclear mechanics. *Mol. Biol. Cell* **31**, 1788–1801 (2020).
35. P. Scaffidi, T. Misteli, Lamin A-dependent misregulation of adult stem cells associated with accelerated ageing. *Nat. Cell Biol.* **10**, 452–459 (2008).

36. B. Kc, D. G. May, B. V. Benson, D. I. Kim, W. G. Shivega, M. H. Ali, R. S. Faustino, A. R. Campos, K. J. Roux, VRK2A is an A-type lamin-dependent nuclear envelope kinase that phosphorylates BAF. *Mol. Biol. Cell* **28**, 2241–2250 (2017).
37. A. D. Elliott, Confocal microscopy: Principles and modern practices. *Curr. Protoc. Cytom.* **92**, e68 (2020).
38. H. Pan, Y.-K. Choi, Y. Liu, W. Hu, Q. Du, K. Polthier, C. Zhang, W. Wang, Robust modeling of constant mean curvature surfaces. *ACM Trans. Graph.* **31**, 1–11 (2012).

Acknowledgments
Funding: This work was supported by the National Institutes of Health grant U01 CA225566 (to T.P.L. and R.B.D.), the Cancer Prevention and Research Institute of Texas Established Investigator award RR200043 (to T.P.L.), the National Science Foundation awards 2412520 and 2226157 (to T.P.L.), and 2226156 to R.B.D. **Author contributions:** Conceptualization: B.M., K.H., R.B.D., and T.P.L. Methodology: B.M., K.H., R.B.D., and T.P.L. Software: B.M., T.-C.W., K.H., and R.B.D. Validation: B.M., S.A., K.H., M.M., R.B.D., and T.P.L. Formal analysis: B.M., S.A., T.-C.W., K.H., M.M., and R.B.D. Investigation: B.M., S.A., T.-C.W., K.H., S.K., R.B., K.B.M., and M.M. Resources: R.B.D., T.P.L. Data curation: T.-C.W., K.H., and T.P.L. Writing—original draft: B.M., T.-C.W., R.B.D., T.P.L. Writing—review and editing: B.M., S.A., T.-C.W., R.B.D., and T.P.L. Visualization: B.M., S.A., T.-C.W., K.H., M.M., R.B.D., and T.P.L. Supervision: S.A., K.H., R.B.D., and T.P.L. Project administration: S.A., K.H., R.B.D., and T.P.L. Funding acquisition: R.B.D. and T.P.L. **Competing interests:** The authors declare that they have no competing interests. **Data and materials availability:** All data needed to evaluate the conclusions in the paper are present in the paper and/or the Supplementary Materials.

Submitted 26 August 2024
Accepted 25 February 2025
Published 28 March 2025
10.1126/sciadv.ads6573